Journal of
Marine Science and Engineering

MDPI

Article

Development and Characterization of 3D-Printable PA6/Oyster Shell Composites for Potential Oyster Spat Collector Applications

Julia Tetzner *, Thomas Potempa, Max Juraschek and Max Ehleben

Institute of Recycling, Ostfalia University of Applied Sciences, Robert-Koch-Platz 10–14, 38440 Wolfsburg, Germany; potempa@ostfalia.de (T.P.); m.juraschek@ostfalia.de (M.J.); m.ehleben@ostfalia.de (M.E.)
* Correspondence: ju.tetzner@ostfalia.de

Abstract

The growing accumulation of plastics in marine environments and their fragmentation into microplastics have increased the demand for durable and sustainable materials for aquaculture applications. Oyster shell waste is particularly attractive because it is an abundant by-product of shellfish aquaculture and consists predominantly of biogenic calcium carbonate ($CaCO_3$), a mineral naturally associated with oyster habitats. This study investigates the feasibility of incorporating oyster shell powder into polyamide 6 (PA6) to produce 3D-printable composites for potential oyster spat collector applications. PA6 composites containing 10, 20, and 30 wt% oyster shell powder were compounded, extruded into filaments, and processed via fused deposition modeling (FDM). The materials were characterized with respect to processability, thermal and mechanical properties, moisture uptake, filler composition, and $CaCO_3$ dissolution behaviour. All formulations showed good processability and were successfully printed into mechanically stable specimens. Increasing filler content increased stiffness but reduced ductility, while melting and crystallization temperatures remained largely stable but influenced enthalpy properties at higher filler loadings. Immersion experiments revealed partial dissolution of the mineral phase, indicating partial $CaCO_3$ dissolution without visible degradation of the PA6 matrix. Overall, the results demonstrate the feasibility of highly filled PA6/oyster shell composites for additive manufacturing and provide a foundation for future studies addressing seawater exposure, oyster larval settlement and field-scale validation.

Keywords: polyamide 6; oyster shell waste; biocomposite; additive manufacturing

Check for updates

Academic Editor: Azizur Rahman

Received: 14 October 2026
Revised: 1 November 2026
Accepted: 6 November 2026
Published: 8 November 2026

Copyright: © 2026 by the authors. Licensee MDPI, Basel, Switzerland. This article is an open access article distributed under the terms and conditions of the Creative Commons Attribution (CC BY) license.

1. Introduction

Plastic pollution and the accumulation of plastic waste in marine environments have intensified the need for sustainable, durable, and environmentally compatible materials in aquaculture systems. Oyster farming particularly depends on artificial settlement substrates ("spat collectors"), which should combine mechanical robustness, environmental compatibility, and biological functionality. Traditional collectors, including mesh bags, plastic bottles, cement-coated structures, and "Chinese hats", support larval settlement through their geometry and surface properties [1,2]. Challenges like low durability, limited recyclability, and high replacement rates contribute over time to microplastic generation in coastal ecosystems [3] and drive the search for safer and more circular materials aligned with sustainability frameworks. At the same time, the oyster industry generates large amounts of shell waste that are often disposed of or used in low-value applications. Oyster shells

consist predominantly of biogenic calcium carbonate ($CaCO_3$) [4,5] and therefore represent a promising secondary raw material. Previous research has demonstrated that shell-derived $CaCO_3$ can be used as a functional filler in thermoplastic polymers (see Table 1). Comprehensive reviews by Owuamanam and Cree (2020) [6] and Azarian and Sutapun (2022) [4] showed that biogenic calcium carbonate obtained from shell waste generally improves stiffness, hardness, and dimensional stability while reducing the dependence on virgin mineral fillers and supporting resource-efficient material concepts. Similar effects have been reported in oyster shell-filled polyolefins. Benaichouba et al. (2025) [5] and Bouiadjra et al. (2024) [7] observed increased stiffness, dimensional stability, and thermal resistance in polypropylene-based composites, whereas Shah et al. (2018) [8] highlighted the importance of particle size, distribution of filler particles in the polymer matrix and interfacial adhesion for the resulting mechanical performance. In addition, Qu et al. (2023) [9] reported modifications of crystallinity and thermal behaviour in oyster shell-filled polyethylene, which were attributed to the nucleating effect of biogenic calcium carbonate. Collectively, these studies demonstrate that oyster shell-derived $CaCO_3$ can provide both mechanical reinforcement and functional modifications across a wide range of polymer systems.

Polyamide 6 (PA6) is a widely used engineering thermoplastic characterized by high strength, abrasion resistance, and good durability under aquatic exposure [10–12]. Although PA6 is hygroscopic and sensitive to moisture uptake, it exhibits comparatively low degradation rates in aquatic environments [10] and can be successfully recycled into mechanically robust products [11]. The incorporation of mineral fillers is a common strategy for modifying thermoplastic properties and reducing material costs [8,12–15]. In particular, Harikumar et al. (2023) [15] demonstrated the successful incorporation of oyster shell-derived $CaCO_3$ into PA6 and reported promising tribological performance. However, their work focused on conventionally manufactured specimens and did not investigate filament production, FDM processing, moisture uptake, thermal behaviour, or mineral-dissolution phenomena.

In parallel, fused deposition modelling (FDM) has become increasingly attractive for the production of customized polymer structures due to its design flexibility and ability to manufacture complex geometries. For example, Sharvesh et al. (2025) [16] demonstrated that optimized printing parameters can significantly improve the mechanical and tribological performance of carbon-fibre-reinforced PA6 through enhanced interlayer bonding. However, highly filled polymer composites remain challenging to process because filler content directly influences melt viscosity, interlayer adhesion, and defect formation [12,16]. Although oyster shell-containing composites have already been investigated in polymer systems and additive-manufacturing applications, important knowledge gaps remain. Romario et al. (2024) [17] demonstrated the incorporation of oyster shell waste into additively manufactured clay-based composites. However, neither polymer processing, filament extrusion, nor thermoplastic FDM systems were considered.

Consequently, systematic investigations of highly filled (>20 wt%) PA6/oyster shell composites covering the complete process chain from compounding and filament extrusion to FDM processing, thermal and mechanical characterisation, moisture uptake, elemental analysis, and mineral-dissolution behaviour remain largely absent from the literature.

Beyond the technical development of the composite, the present work was motivated by principles of the Safe and Sustainable by Design (SSbD) framework, which promotes resource efficiency, circularity, and reduced environmental impacts throughout the material life cycle [18–21]. Oyster shell-derived calcium carbonate represents an attractive secondary raw material because it valorises an abundant aquaculture by-product while partially replacing conventional mineral fillers [4,6]. In combination with the design flexibility of additive manufacturing, this approach addresses selected SSbD principles at the material-

design level through waste valorisation, resource efficiency, and the development of durable, additively manufacturable composites. However, no formal SSbD assessment, life-cycle assessment, ecotoxicological evaluation, or long-term marine exposure study was performed. Therefore, SSbD should be regarded as a design motivation rather than a demonstrated material property.

Table 1. Comparison of representative studies on oyster shell, $CaCO_3$-filled polymers or PA6 composites for FDM/additive manufacturing.

Reference	Matrix	Filler Loading	Particle Size	Processing	Key Characterisation
Shah et al. [8]	PP	0–50 wt%	3; 15 µm	Twin-screw + injection moulding	Tensile, flexural, Izod, flame
Benaichouba et al. [5]	PP	10 & 30 wt%	<200 µm	Twin-screw + injection moulding	DSC, TGA, tensile, DMA, SEM
Qu et al. [9]	LDPE	10–60 wt%	<10 µm	Torque rheometer + hot press	Tensile, WVP, antibacterial
Harikumar et al. [15]	PA6	Not specified	n.s.	Conventional (non-FDM)	Wear, COF
Romario et al. [17]	Clay/ polymerhybrid	Not specified	n.s.	FDM (AM)	None (proof-of-concept)
Sharvesh et al. [16]	PA6	20 wt% CF	n.s.	FDM (Snapmaker)	Hardness, tensile, impact, wear
Present study	PA6	10, 20, 30 wt%	<250 µm	Twin-screw + FDM	TGA, DSC, tensile, moisture, LIBS, immersion

Against this background, a clear research gap exists in the systematic investigation of highly filled, additively manufacturable PA6 composites containing oyster shell-derived $CaCO_3$ for aquaculture applications. While previous studies have demonstrated the feasibility of oyster shell fillers in polymer composites and additive-manufacturing applications, comprehensive investigations of highly filled PA6/oyster shell systems remain largely absent. In particular, no study has systematically examined filler contents up to 30 wt% across the complete manufacturing chain, including compounding, filament extrusion, FDM processing, thermal and mechanical characterization, moisture uptake, and mineral-dissolution behaviour. Accordingly, the novelty of the present work lies in the integrated investigation of highly filled PA6/oyster shell composites from material preparation and filament production to FDM processing and performance characterization. Additionally, accelerated $CaCO_3$ dissolution experiments are introduced as a first step towards evaluating the application-relevant behaviour of shell-filled PA6 composites for future aquaculture structures.

The present study focuses on material development and characterization. Biological functionality, oyster larval settlement, and collector performance under marine conditions are beyond the scope of this work and require dedicated investigation in future studies. Accordingly, this study pursues three objectives: (i) to evaluate the processability and mechanical performance of highly filled PA6/oyster shell composites manufactured via FDM, (ii) to establish suitable compounding, filament-extrusion, and FDM-processing parameters for filler contents up to 30 wt% and (iii) to investigate $CaCO_3$ dissolution behaviour as a material characteristic relevant to the future development of shell-containing aquaculture structures.

2. Materials and Methods

2.1. Materials

Commercial polyamide 6 (Ultramid® B50L01, BASF) was used as the polymer matrix. PA6 was selected for its high strength, abrasion resistance, proven stability under marine exposure and its common use in marine applications.

Oyster shells were obtained from OYTA (Denmark), where they are sold as a natural calcium supplement for animals. No chemical, thermal, or cleaning pretreatment was applied prior to processing. The shells were mechanically milled and classified as described in Section 2.2. A composition analysis was performed using LIBS (Section 2.6). The final filler fraction (<0.25 mm) was used for masterbatch production and composite preparation.

2.2. Material Preparation

Raw oyster shells were mechanically processed to obtain a particle size of 0.25 mm, suitable for twin-screw extrusion and FDM printing. Coarse grinding was performed using a cross-beater mill (RETSCH SK 1000 Comfort, 1 mm sieve), followed by further size reduction in a knife mill. After each grinding step, particle fractions were classified using a RETSCH VS 1000 sieve tower (1.0–0.1 mm, 5 min). Oversized fractions were re-milled until a stable particle size was achieved. A masterbatch U70/30 containing 30 wt.% oyster shell powder was produced as the basis for compounds with lower filler contents. Extrusion was performed according to DIN EN ISO 16396-2 using a co-rotating twin-screw extruder (Leistritz ZSE 40 GL 40 D) with gravimetric feeding. After drying the materials at 80 °C for at least 5 h, extrusion was carried out at zone temperatures of 210–245 °C and a discharge temperature of 258 °C. Mass-flow rates were adjusted to 10.5 kg/h for the polymer and 4.5 kg/h for the shell powder, while the screw speed was maintained at 155 rpm. Filler introduction occurred at a downstream point within the melt to ensure homogeneous distribution across the matrix. After extrusion, the material was pelletized.

Filaments suitable for 3D printing were produced using a Brabender extruder (Type 837410) in combination with a Scheer SGS 25-E4 granulator without a cutting unit. The U80/20 and U90/10 compounds were obtained by homogenously blending the 70/30 masterbatch with defined amounts of neat PA6. Specifically, U80/20 was produced from 0.5 kg U70/30 and 0.25 kg PA6, whereas U90/10 was prepared from 0.5 kg U70/30 and 1 kg PA6. The extrusion temperature profile (220–240 °C) corresponded to the masterbatch conditions. A filament diameter of 2.85 mm was achieved by adjusting the screw speed while maintaining a constant granulator speed of 14 rpm. Processing speeds were 40 rpm for U70/30, 34 rpm for U80/20, and 27 rpm for U90/10. All formulations produced continuous, dimensionally stable filaments with a diameter tolerance of ±0.05 mm and without visible surface defects.

2.3. 3D Printing

Fused Deposition Modelling (FDM) was performed using an Ultimaker 3 printer equipped with a 0.4 mm nozzle (Print Core AA). For each formulation, ten Type 1A tensile specimens (DIN EN ISO 527-1) and one demonstrator-scale oyster spat collector (diameter: 9 cm; height: 1.5 cm) were printed. Five additional specimens were produced as reserve samples to compensate for potential printing defects and to allow selection of geometrically conforming specimens for mechanical testing. Due to the hygroscopic nature of PA6, all filaments were dried at 80 °C for 16 h prior to printing. The optimized printing parameters were a nozzle temperature of 255 °C, a build-plate temperature of 115 °C, a printing speed of 40 mm s^{-1}, a layer height of 0.30 mm, and a material flow of 195%. Tensile specimens were printed with 100% triangular infill, whereas collector demonstrators were printed with 80% infill to reduce material consumption. Cooling was disabled and build-plate adhesion was enhanced using a glue-coated build plate and a brim.

2.4. TGA

To verify mixing ratios, TGA was performed per DIN EN ISO 11358-1, using a NETZSCH TG 209 F1 Iris system. Five samples per material (20 mg each) were analyzed in N_2 at 20 K/min from 50 °C to 600 °C.

2.5. DSC

Thermal properties and crystallinity were analysed via DSC, using a NETZSCH DSC 214 Polyma. According to ASTM D3418, measurements were performed with a heating rate of 10 K/min and in a temperature range from 50 °C to 250 °C, under a nitrogen atmosphere and with isothermal steps between each dynamic step to ensure the sample temperature. The average weight of the sample was about 10 mg and samples were sealed in perforated aluminum vessels. The exothermic peak minimum and endothermic peak maximum (second heating) were taken as crystallization and melting temperatures (T_C and T_m), whereas the area of each peak was considered as the crystallization and melting enthalpy (ΔH_C and ΔH_m). To determine the crystallinity (X_C), the following formula was used:

$$X_C = \frac{\Delta H_m}{\Delta H_m^0 \times w_p} \times 100\% \quad (1)$$

With ΔH_m = measured melting enthalpy (second heating), ΔH_m^0 is the enthalpy of 100% crystalline PA6 (230 J/g) [22] and w_p is the measured PA6 mass fraction from TGA (71.4, 80.6 and 87.1 wt% for U70/30, U80/20 and U90/10, respectively; Section 3.2). No cold-crystallisation peak was observed during the second heating cycle. Consequently, the degree of crystallinity was calculated solely from the melting enthalpy and corrected for the measured polymer mass fraction.

2.6. Microscopy and Elemental Analysis

Laser-induced breakdown spectroscopy (LIBS) was performed using a KEYENCE EA-300 VHX microscope to characterize the elemental composition of particulate inclusions within the PA6 matrix. Three visually distinct particle types (red, orange, and white) were analyzed using 15 laser pulses per particle group. A solid PA6 region and a biogenic $CaCO_3$ reference (mussel shell, used solely as a compositional benchmark for Ca-rich marine carbonates) served as reference materials. Due to potential interference from atmospheric nitrogen and the limited sensitivity for trace elements, nitrogen-containing species and low-concentration elements were not quantitatively evaluated.

2.7. Moisture Absorption

Moisture content was determined using a HydroTracer FVL (Aboni), with two replicate measurements per blend. Samples were conditioned at 65 ± 5% relative humidity and 23 ± 2 °C for 72 h and measured immediately afterwards. Due to the limited number of replicates ($n = 2$), no inferential statistical testing was performed, and values are reported descriptively.

2.8. Mechanical Properties

Mechanical properties were determined by tensile testing according to DIN EN ISO 527-1. Ten Type 1A specimens were printed per formulation to allow selection of five specimens based on visual inspection for geometric conformity and absence of visible delamination or warping. All test specimens per formulation were printed sequentially within a single continuous print run from the same filament spool (same batch). Accordingly, five type 1A 3D-printed specimens per blend were tested on a Zwick/Roell BZ1-MM14450.ZW06, using VideoXtens for strain measurement and TestXpert III V1.4 software for data analysis.

A pre-force of 10 N was applied; the modulus was determined using a crosshead speed of 1 mm/min, and tensile strength was measured at 5 mm/min. Yield strength and failure were reported per DIN EN ISO 527-1: where no distinct yield point was detected (brittle fracture), σ_Y was taken as the maximum stress ($\sigma_Y = \sigma_M = \sigma_B$); where a yielding event was present, σ_Y was reported at the local stress maximum preceding a force drop exceeding 5%. Reported values include Young's modulus, yield strength, and elongation at yield, expressed as mean ± standard deviation.

2.9. Immersion Test

The immersion test was performed following the principles of DIN EN ISO 16888-1 and -2, which define the exposure of a polymer specimen to a chemical medium under controlled conditions and the subsequent assessment of mass change and visual appearance as indicators of chemical resistance. For each composite, two types of samples were tested: (1) extruded filament segments (5.0 ± 0.1 g) and (2) FDM-printed Type 1A specimens. Five replicates per form ($n = 5$) were immersed in 50 mL 1 M acetic acid in Erlenmeyer flasks with a magnetic stir bar for 72 h under stirring at 120 rpm and at ambient laboratory temperature (21 ± 2 °C). After immersion, samples were rinsed five times with deionised water, dried at 80 °C, and reweighed. The residual mixture proportions were quantified by TGA. Two calculation approaches were applied to estimate mineral loss. In Method 1, the total specimen mass loss was attributed entirely to dissolution of the oyster shell fraction, assuming an inert PA6 matrix (chemical-resistance class A for dilute acetic acid) (see Formula (2)). In Method 2, the dissolved mineral mass was calculated from the TGA-determined shell fractions before and after immersion and therefore accounts for changes in composite composition during exposure (see Formula (3)). Method 1 is regarded as a conservative lower-bound estimate, whereas Method 2 is considered the best available approximation of actual mineral dissolution under the applied test conditions.

$$\Delta m_{shell,lower} = \frac{\Delta m_{sample}}{m_{sample_0} \times wt\%_{shell_0}} \times 100\% \quad (2)$$

$$\Delta m_{shell,TGA} = \frac{\left(m_{sample_0} \times wt\%_{shell_0} - m_{sample_1} \times wt\%_{shell_1}\right)}{m_{sample_0} \times wt\%_{shell_0}} \times 100\% \quad (3)$$

Since dissolved Ca^{2+} was not quantified in the immersion solution, the calculated values represent estimated mineral loss based on solid-phase mass balances rather than direct calcium release. Small apparent increases in calculated PA6 mass after immersion were within the combined uncertainty of weighing, drying, and TGA measurements and were therefore not interpreted as actual polymer mass gain. Visual assessment included inspection for surface leaching, color gradients, and deposition of calcium-containing residues; all observations were documented photographically. As the intended application involves marine environments, an accelerated laboratory test was used to evaluate whether calcium-containing phases can be released from the composite matrix. Acetic acid was selected as a standardized and reproducible medium that promotes $CaCO_3$ dissolution while preserving PA6 (chemical-resistance class A for diluted acetic acid) [23]. The immersion test was not intended to simulate seawater conditions but rather to compare the relative release behaviour of the different formulations.

3. Results

All results are reported as mean ± standard deviation unless otherwise stated. All quantitative datasets were analysed via ANOVA (including Levene's test for homogeneity) with Tukey's HSD applied when Levene's test was non-significant, and Games–Howell addi-

tionally reported when Levene's test was significant ($\alpha = 0.05$). Raw and processed data files are available as Supplementary Material, supporting full reproducibility and transparency.

3.1. Filament Production and Process Stability

All three PA6/oyster shell composites (10, 20, and 30 wt% filler) were successfully compounded and extruded into filaments with a nominal diameter of 2.85 mm (±0.05; manufacturing tolerance window, measured at different positions per spool, no statistical SD). Changes in processing behaviour (extrusion torque and screw speed) suggested an increase in apparent melt viscosity [24], but no strand breakage, nozzle clogging, or granule fragmentation occurred. Visual inspection showed a progressively more opaque filament appearance and no visible surface agglomerates at any filler level. All formulations, including U70/30, remained processable under the applied extrusion conditions.

3.2. Determination of the Mixing Ratios (TGA)

Thermogravimetric analysis confirmed blend composition as follows: U70/30: 71.4/28.6 (±1.6) %, U80/20: 80.6/19.4 (±0.7) % and U90/10: 87.1/12.9 (±0.4) % ($n = 5$). All group differences are statistically significant (ANOVA $p < 0.05$), confirming that increasing the filler fraction leads to a corresponding rise in inorganic residue after thermogravimetric analysis. The low standard deviations observed in the TGA mixing-ratio determination (±1.6, ±0.7, and ±0.4%; $n = 5$) further support a macroscopically homogeneous filler distribution across the extruded pellets. However, these indirect indicators do not replace a direct microscopic assessment of particle dispersion within the filament cross-section; SEM or µCT analysis of polished cross-sections was not performed within the scope of this study.

3.3. 3D Printing

Initial printing trials resulted in severe warping and insufficient layer adhesion under 100% material flow (see Figure 1a), resulting in uneven layer thicknesses across the cross-section (see Figure 1b). Parameter optimisation demonstrated that printing performance was strongly influenced by build-plate temperature, adhesion strategy, and material flow. Stable build-plate adhesion was achieved using a glue-coated build plate and a build-plate temperature of 115 °C. Furthermore, increasing the material flow from 100% to 195% was empirically determined to compensate for the reduced melt flowability of the highly filled composite. As a result, incomplete layers were eliminated, and interlayer bonding improved.



(**a**) (**b**)

Figure 1. 3D printed test specimen with (**a**) incomplete layers under 100% flow and (**b**) different thicknesses over the cross section.

Following optimisation, all formulations were successfully processed into tensile specimens and collector demonstrators (Figure 2). No visible delamination or cracking was observed. Increasing filler content resulted in slightly rougher surfaces, indicating reduced flowability of the highly filled formulations. Nevertheless, all materials remained printable and geometrically stable under the selected processing conditions. The requirement for elevated material flow suggests reduced melt flowability at higher filler loadings. However, no quantitative rheological measurements were performed, and therefore, this interpretation remains qualitative.



Figure 2. Photography of the 3D-printed collector models made of the materials U70/30 (**left**), U80/20 (**middle**), and U90/10 (**right**) (diameter: 9 cm; height: 1.5 cm).

3.4. Moisture Absorption

Moisture measurements yielded values of 0.44 (±0.03) % for U70/30, 0.48 (±0.002) % for U80/20 and 0.54 (±0.01) % for U90/10 (n = 2 each). All values were substantially lower than the 2.6% reported for neat PA6 on the manufacturer datasheet (Ultramid B50L01), indicating reduced moisture uptake in the composites; as with the mechanical data, this comparison is qualitative because no FDM-printed neat PA6 control was tested. Due to the limited number of replicates, these results should be interpreted as preliminary trends.

3.5. Tensile Test

Young's modulus increased with increasing oyster shell content, from 1460 ± 748 MPa for U90/10 to 3120 ± 1228 MPa for U80/20 and 3960 ± 856 MPa for U70/30. Statistical analysis revealed significantly higher modulus values for U80/20 and U70/30 compared with U90/10 ($p < 0.05$), whereas no significant difference was observed between U80/20 and U70/30. The manufacturer-reported Young's modulus of neat PA6 (Ultramid® B50L01; 3000 MPa) is provided solely as an engineering benchmark and not as a direct experimental control, as no FDM-printed neat PA6 specimens were tested under identical conditions. Nevertheless, U80/20 and U70/30 exhibited stiffness values within or above the range reported for the virgin material. Yield strength followed a similar trend, increasing from 28.0 ± 3.3 MPa for U90/10 to 42.6 ± 7.6 MPa and 40.9 ± 10.0 MPa for U80/20 and U70/30, respectively. A statistically significant increase was observed between 10 wt% and 20 wt% filler loading ($p < 0.05$), whereas no significant difference was detected between the 20 wt% and 30 wt% formulations. Despite this improvement, all composites remained below the manufacturer-reported yield strength of neat PA6 (90 MPa). In contrast, elongation at yield decreased from 6.0 ± 8.8% for U90/10 to 1.8 ± 0.6% for U80/20 and 1.4 ± 0.2% for U70/30. However, due to the substantial within-group variability, no statistically significant differences were detected (ANOVA: $p = 0.329$; Games–Howell: all pairwise comparisons $p > 0.49$). The observed decrease in elongation is therefore interpreted as a trend rather than a statistically confirmed effect. Such behaviour is nevertheless consistent with the reduced ductility commonly reported for particle-reinforced thermoplastics [4,21].

The comparatively large scatter observed for U90/10 was primarily caused by two specimens with markedly different stress–strain behaviour. Specimen U90/10-1 exhibited the lowest Young's modulus (306 MPa) and failed in a brittle manner at an elongation of 2.3%, whereas specimen U90/10-4 showed an unusually high elongation at yield of 21.6% and a distinct stress maximum prior to failure. In contrast, the remaining three specimens exhibited comparatively consistent behaviour, with Young's modulus values between 1500 and 2080 MPa, yield strengths ranging from 24.8 to 29.0 MPa, and elongations at yield between 1.6 and 2.4%. Consequently, the large standard deviation observed for U90/10 should be attributed primarily to specimen-to-specimen variability rather than to a systematic material effect.

3.6. DSC

Melting temperature (T_m) averaged 221.5 (±0.1) °C (U90/10), 221.1 (±0.2) °C (U80/20) and 221.4 (±0.2) °C (U70/30). ANOVA was significant ($F(2,6) = 6.00$; $p = 0.037$), with Tukey's HSD confirming a difference only between U80/20 and U90/10 ($p = 0.035$). Crystallisation temperature (T_C) ranged from 186.0 (±0.2) °C (U90/10) to 186.9 (±2.9) °C (U80/20) and 187.0 (±0.1) °C (U70/30). ANOVA was non-significant ($F(2,6) = 0.345$; $p = 0.721$), although Levene's test for homogeneity was significant and Games–Howell post hoc comparisons revealed a significant difference between U70/30 and U90/10. However, for both temperatures (T_m and T_C) the absolute deviations are below 0.47 °C and are therefore of limited practical relevance. In contrast, enthalpy-based parameters showed clear compositional effects. U90/10 exhibited the highest melting enthalpy (72.3 ± 1.1 J/g), followed by U70/30 (62.6 ± 0.3 J/g) and U80/20 (58.9 ± 1.8 J/g). All pairwise comparisons were significant for ΔH_m ($F(2,6) = 97.67$; $p < 0.001$). Similarly, the crystallisation enthalpy showed the highest result at U90/10 with 68.0 (±2.6) J/g, followed by U70/30 with 61.3 (±0.7) J/g and 56.1 (±0.7) J/g for U80/20. ANOVA was significant ($F(2,6) = 41.92$; $p < 0.001$) and, given the significant Levene's test ($p = 0.041$), the Games–Howell comparison additionally showed significant differences between U80/20 and U70/30 as well as U80/20 and U90/10.

After normalization to the measured PA6 mass fraction, the crystallinity (X_C, second heating) was 38.3 (±0.2) % for U70/30, 31.6 (±1.0) % for U80/20 and 36.2 (±0.5) % for U90/10. Consistent with the raw enthalpy values, the crystallinity did not decrease monotonically with filler content; the lowest value was observed at 20 wt% filler.

3.7. Microstructural and Elemental Analysis (Keyence LIBS Microscopy)

The LIBS analysis revealed that all three particle types (red, orange, white; see Figure 3) share a consistent Ca–O–C elemental profile consistent with a calcium-rich carbonate filler phase. The spectra of the red particles were dominated by Ca and O, closely matching the mussel shell reference and supporting their assignment as mineral inclusions. Orange and white particles exhibited similar Ca-rich signatures, with additional C signals that fall within the expected response range of $CaCO_3$. Importantly, elevated carbon intensities were not interpreted as polymer contamination, as $CaCO_3$ intrinsically contains chemically bound carbon and typically yields strong carbon emission lines under LIBS excitation. Only measurement spots showing simultaneous carbon and hydrogen signals suggested local PA6 residues at particle surfaces. Trace elements (Na, K, Fe, F) occurred sporadically across particle types and may be associated with impurities commonly observed in marine carbonate materials [13,24]. Collectively, the results are consistent with a calcium-rich carbonate filler phase originating from the oyster shell feedstock.



Figure 3. Microscopic photo of U70/30 filament with orange, white, and red particles.

3.8. $CaCO_3$ Dissolution and Mineral Release

All composites exhibited partial dissolution of the mineral fraction when immersed in 1 M acetic acid for 72 h. Due to the higher initial mineral content, U70/30 exhibited the greatest absolute mineral loss (0.29 g according to Method 2), followed by U80/20 (0.24 g) and U90/10 (0.17 g). Method 1 yielded mineral-loss values of 14.7%, 15.5%, and 15.5% for U70/30, U80/20, and U90/10, respectively. Method 2 resulted in higher estimates of 20.3%, 24.7%, and 26.6% (see Table 2).

Table 2. Averaged mixing ratios of the U70/30, U80/20 and U90/10 filaments in % and weights of oyster shells before and after the immersion test, with the respective standard deviation ($n = 5$).

Filament		Mixing Ratio PA6/Oyster Shell [%] *	Weight Sample [g]	Weight Oyster Shell [g]	Δw Oyster Shell Fraction ** [%]	Δw Oyster Shell Fraction *** [%]
U70/30	before	71.4/28.6 (±1.6)	5	1.43 (±0.08)		
	after	76.2/23.8 (±1.1)	4.79	1.14 (±0.06)	14.7	20.3
U80/20	before	80.6/19.4 (±0.7)	5	0.97 (±0.04)		
	after	84.9/15.1 (±0.4)	4.85	0.73 (±0.02)	15.5	24.7
U90/10	before	87.1/12.9 (±0.4)	5	0.64 (±0.02)		
	after	90.5/9.5 (±0.6)	4.9	0.47 (±0.03)	15.5	26.6

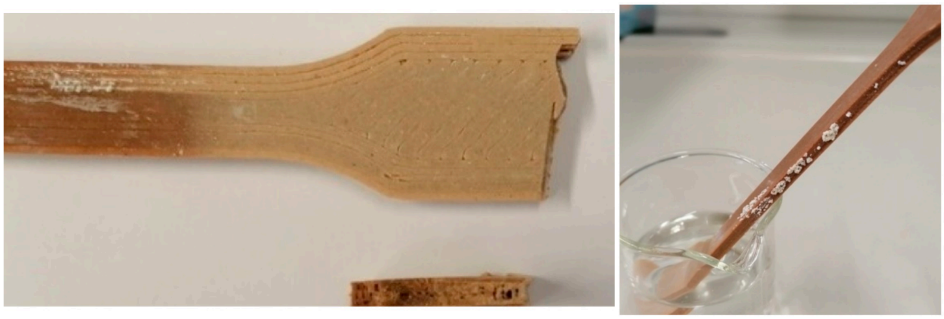
* Mixing ratio from TGA measurement (chapter 3.2); ** according to formula (2); *** according to TGA mixing ratios and formula (3).

The discrepancy between both approaches is attributed to apparent increases in the calculated PA6 mass after immersion, which are physically implausible for a chemically resistant PA6 matrix and are therefore interpreted as measurement artefacts. Potential sources of uncertainty include residual bound moisture, retention of calcium-containing reaction products, weighing uncertainty, and local compositional heterogeneity. For example, a U70/30 specimen initially contained 1.43 g oyster shell (5.00 g × 28.6 wt%). After immersion, the shell content decreased to 1.14 g (4.79 g × 23.8 wt%), corresponding to a calculated mineral loss of 0.29 g and a dissolution fraction of 20.3%. Using the total specimen mass loss only, the same specimen yielded a dissolution estimate of 14.7%.

$$\Delta m_{shell,lower}(U70/30) = \frac{0.21\ g}{5\ g \times 0.286} \times\ 100\% = 14.7\% \quad (4)$$

$$\Delta m_{shell,TGA}(U70/30) = \frac{(5\ g \times 0.286 - 4.79\ g \times 0.238)}{5\ g \times 0.285} \times 100\% = 20.3\% \quad (5)$$

Printed specimens showed similar trends but lower absolute loss, which may be partly attributed to the reduced accessible surface area of the printed geometry (no direct surface-area measurement was performed). ANOVA on post-immersion mixing ratios confirmed significant differences between formulations for both filaments and printed specimens ($p < 0.001$). Distinct color gradients were visible across the samples' cross-sections, indicating preferential leaching from external regions (see Figure 4a). This inhomogeneity contributes to greater measurement variation when samples from both regions are analyzed. Surface residues and white deposits were also observed at all compositions (see Figure 4b) and are most plausibly attributed to recrystallised calcium salts formed during drying, although their exact composition was not analysed. These effects were most pronounced in U70/30 and diminished with decreasing filler content. Macroscopic dimensional changes could not be quantified with precision, but visual inspection indicated no obvious geometric deformation, which should be confirmed by measurements in future work.



(a) (b)

Figure 4. U70/30 test specimen after immersion test in acetic acid with (**a**) colour gradient and (**b**) calcium deposits.

4. Discussion

The present study demonstrates the feasibility of producing highly filled PA6/oyster shell composites containing up to 30 wt% biogenic $CaCO_3$ via compounding, filament extrusion, and fused deposition modeling. Despite the relatively high filler loading and the absence of shell pretreatment or compatibilization, all formulations could be processed into continuous filaments and mechanically stable printed structures. Increasing filler content resulted in higher melt viscosity and extrusion torque, as commonly observed for mineral-filled thermoplastics [25], but no critical extrusion problems such as strand breakage or nozzle clogging occurred. The successful production of demonstrator-scale collector geometries further highlights the potential of additive manufacturing for customized aquaculture structures and rapid design adaptation.

The printing experiments showed that process optimization was essential for achieving adequate print quality. Severe warping and poor interlayer bonding occurred during initial trials but were successfully mitigated through adjustments to build-plate temperature, adhesion, and material flow. The requirement to increase material flow to 195% suggests reduced flowability and incomplete layer fusion at standard settings, which is consistent with previous observations for highly filled FDM materials [12,26]. Although surface roughness and micro-porosity increased with filler content, all formulations remained printable and structurally stable. This finding is particularly relevant given that high filler loadings are typically associated with reduced printability and increased defect formation.

The mechanical results demonstrated the typical behavior of mineral-filled thermoplastics. Increasing filler content significantly increased stiffness, while ductility decreased. Although yield strength improved between 10 and 20 wt% filler, all composites remained below the manufacturer-reported yield strength of neat PA6 (90 MPa). The mechanical properties of neat PA6 reported by the manufacturer were used as an engineering benchmark rather than as a direct experimental control. The primary objective of this study was to evaluate the feasibility of highly filled PA6/oyster shell composites and to assess whether the resulting materials retain property levels that are relevant for potential aquaculture applications. Consequently, comparisons with neat PA6 are intended to provide context regarding the typical performance range of the virgin material. However, because no FDM-printed neat PA6 specimens were produced and tested under identical conditions, these comparisons should be interpreted qualitatively rather than quantitatively. The yield-strength discrepancy nevertheless indicates limited stress transfer between matrix and filler. This behaviour, whereby the E-modulus increases while the yield strength and elongation decrease, is typical of the mechanical behaviour of plastics reinforced with three-dimensional particles [27]. However, the large scatter observed in some datasets, particularly for U90/10, suggests that FDM-related factors such as porosity, interlayer adhe-

sion, moisture variations, and possible filler agglomeration contribute substantially to the mechanical response. These observations are consistent with previous studies on mineral-filled FDM polyamides, where stiffness improvements are often accompanied by reduced elongation and increased sensitivity to printing-related defects [12,16]. Furthermore, the absence of shell cleaning or surface treatment may have limited interfacial bonding. The low TGA standard deviations (≤1.6%, Section 3.2) suggest good macroscopic filler homogeneity across the extruded pellets; however, the large mechanical scatter observed in some datasets—particularly U90/10—indicates that microscale dispersion defects (incomplete interlayer fusion, local agglomerates) cannot be excluded without SEM or µCT cross-section analysis. Additional microstructural analyses are therefore required to verify local filler distribution and failure mechanisms.

Thermal analysis showed that oyster shell addition had only a minor effect on melting and crystallization temperatures, which remained close to those of neat PA6. The raw enthalpy-based parameters did not decrease monotonically but were lowest at 20 wt% and partially recovered at 30 wt%. After normalisation to the measured PA6 mass fraction, the apparent crystallinity likewise showed a non-monotonic trend, with the highest value for the most highly filled composite (U70/30). This is consistent with the well-established nucleating effect of $CaCO_3$, which can increase the crystalline fraction of PA6 [4,10]. The raw enthalpy decrease at intermediate loading is therefore dominated by dilution of the polymer phase due to the added shell powder rather than by a genuine loss of crystallinity. It should also be noted that the melting enthalpy determined by DSC does not necessarily reflect the crystallinity present in the FDM-printed tensile specimens themselves. Recent work by Renganathan and Saritha [28] has shown that printing parameters, particularly printing speed, can significantly influence crystallisation behaviour in FDM-processed polymers, leading to crystallinity levels that may differ from those measured on bulk DSC samples. This effect warrants further investigation to directly assess how printing conditions shape the crystalline morphology and consequently the mechanical performance of the printed PA6/oyster shell composites. Moisture uptake was lower than reported for neat PA6, which may result from the reduced fraction of hygroscopic polymer and could provide benefits for filament handling, storage, and dimensional stability. However, the limited number of replicates means that these observations should be regarded as preliminary.

LIBS analysis indicated a Ca-rich elemental profile consistent with the original filler; however, elemental spectroscopy alone cannot confirm carbonate phase identity or prove that the mineral remained chemically intact during compounding at 255 °C. XRD or FTIR measurements to verify calcite/aragonite phase preservation after twin-screw compounding at 255 °C were not performed within the scope of this study and represent a recognised limitation. Such phase-specific analyses should be included in follow-up work to confirm that the $CaCO_3$ crystalline structure was not altered during melt processing. This is important because $CaCO_3$ contributes not only to composite stiffening but also to the release behavior investigated in the immersion experiments. Depending on the evaluation approach, the immersion experiments indicated mineral losses between approximately 15% and 27%. The TGA-corrected mass balance yielded values between 20.3% and 26.6% and is therefore considered the most realistic estimate of mineral dissolution under the applied test conditions. Despite the observed mineral loss, the PA6 matrix remained visually intact and no obvious macroscopic deformation was detected. Small apparent increases in calculated PA6 mass are attributed to measurement uncertainty, residual moisture, retained reaction products, or local compositional heterogeneities and should not be interpreted as actual polymer mass gain. The observed color gradients and surface deposits suggest that dissolution primarily occurred in regions where filler particles were exposed or located close to the surface. Although the acetic acid test was not intended to simulate seawater conditions, it demonstrates

that calcium-containing species can be mobilized from the composite without complete matrix degradation. Given that oyster larvae naturally encounter calcium-carbonate-rich substrates in reef environments [1], this behavior may be relevant for future collector development. However, any connection between the observed mineral dissolution and oyster larval attachment remains speculative and requires dedicated seawater-exposure studies before functional relevance can be assessed, since no biological settlement experiments were conducted in the present study. The present work should therefore be regarded as a material-level proof-of-concept rather than a validation of collector functionality. While the observed mineral release and successful fabrication of collector-scale structures may be relevant for future applications, no conclusions can be drawn regarding oyster larval settlement, recruitment efficiency, or collector performance under marine conditions.

From a Safe and Sustainable by Design (SSbD) perspective, the composites investigated in this study contribute to several key design objectives, including waste valorization, resource efficiency, circularity, and material durability. The use of oyster shell waste as a functional filler creates value from an abundant aquaculture by-product while partially reducing reliance on virgin raw materials. Furthermore, additive manufacturing facilitates the production of customized structures with potentially reduced material consumption and increased design flexibility. Combined with the long service life and recyclability of PA6, these characteristics highlight the potential of the material system as a more circular alternative for future aquaculture applications. Nevertheless, the present study addresses SSbD principles only at a material-design level. Key aspects, including environmental safety, ecotoxicological effects, long-term degradation behaviour, and life-cycle performance, remain subject to future investigation and are required for a comprehensive SSbD assessment.

The results demonstrate successful processing, increased stiffness, $CaCO_3$ dissolution capability, and the ability to fabricate collector-scale structures. Future work should focus on long-term seawater exposure, oyster larval settlement experiments, biofouling behavior, and field-scale validation to determine the suitability of these materials for practical spat collector applications.

5. Conclusions

This study investigated highly filled PA6/oyster shell composites containing up to 30 wt% oyster shell powder as candidate materials for future oyster spat collector applications. All formulations were successfully compounded, extruded into filaments, and processed via fused deposition modeling, demonstrating the technical feasibility of incorporating substantial amounts of waste-derived $CaCO_3$ into additively manufactured PA6 composites. The addition of oyster shell filler increased stiffness while reducing ductility, reflecting the typical behavior of mineral-filled thermoplastics. Absolute performance was assessed qualitatively against manufacturer data for neat PA6, as no FDM-printed neat PA6 control was included. Thermal analysis showed only minor effects on melting and crystallization temperatures, whereas normalised enthalpy-based crystallinity showed a non-monotonic, and on the polymer-mass basis essentially comparable, level across the three formulations. LIBS measurements showed a Ca-rich elemental profile consistent with the original filler, although phase identity and processing stability cannot be confirmed by elemental spectroscopy alone. Furthermore, immersion experiments demonstrated partial $CaCO_3$ mobilisation from the composite, while no visible macroscopic deformation of the PA6 matrix was observed (quantitative structural stability was not measured).

Beyond the material performance, the investigated system combines additive manufacturing with the valorization of an abundant aquaculture by-product, thereby supporting more circular and Safe-and-Sustainable-by-Design material concepts for marine applica-

tions. The successful fabrication of collector-scale demonstrators further highlights the potential of the approach for customized and application-specific aquaculture structures.

Overall, the results establish a material-level proof of concept for PA6/oyster shell composites and their manufacturability via FDM. However, the present work represents an initial feasibility study rather than a validation of collector performance. Future research should therefore focus on long-term seawater exposure, $CaCO_3$ dissolution kinetics under marine conditions, larval settlement experiments, biofouling behavior, and field-scale deployment to assess the suitability of these materials for practical aquaculture applications.

Supplementary Materials: The following supporting information can be downloaded at: https://www.mdpi.com/article/10.3390/jmse14212121/s1. Table S1: TGA raw data of U70/30 mixing ratio (n = 5); Table S2: TGA raw data of U80/20 mixing ratio (n = 5); Table S3: TGA raw data of U90/10 mixing ratio (n = 5); Table S4: ANOVA: TGA mixing ratio; Table S5: Levene's test: TGA mixing ratio; Table S6: Tukey's HSD: TGA mixing ratio; Table S7: Moisture absorption raw data (n = 2 per formulation); Table S8: Tensile test raw data for U70/30 (n = 5); Table S9: Tensile test raw data for U80/20 (n = 5); Table S10: Tensile test raw data for U90/10 (n = 5); Table S11: ANOVA: Young's modulus; Table S12: Levene's test: Young's modulus; Table S13: Tukey's HSD: Young's modulus; Table S14: ANOVA: yield strength; Table S15: Levene's test: yield strength; Table S16: Tukey's HSD: yield strength; Table S17: Games-Howell post-hoc comparisons: yield strength; Table S18: ANOVA: elongation at yield; Table S19: Levene's test: elongation at yield; Table S20: Tukey's HSD: elongation at yield; Table S21: Games-Howell post-hoc comparisons: elongation at yield; Table S22: DSC raw data (Tm, ΔHm, TC, ΔHc, crystallinity); Table S23: ANOVA: DSC melting temperature; Table S24: Levene's test: DSC melting temperature; Table S25: Tukey's HSD: DSC melting temperature; Table S26: ANOVA: DSC melting enthalpy; Table S27: Levene's test: DSC melting enthalpy; Table S28: Tukey's HSD: DSC melting enthalpy; Table S29: ANOVA: DSC crystallisation temperature; Table S30: Levene's test: DSC crystallisation temperature; Table S31: Tukey's HSD: DSC crystallisation temperature; Table S32: Games-Howell post-hoc comparisons: DSC crystallisation temperature; Table S33: ANOVA: DSC crystallisation enthalpy; Table S34: Levene's test: DSC crystallisation enthalpy; Table S35: Tukey's HSD: DSC crystallisation enthalpy; Table S36: Games-Howell post-hoc comparisons: DSC crystallisation enthalpy; Table S37: ANOVA: DSC crystallinity; Table S38: Levene's test: DSC crystallinity; Table S39: Tukey's HSD: DSC crystallinity; Table S40: LIBS elemental analyses of "red" particles (15 scans); Table S41: LIBS elemental analyses of "orange" particles (15 scans); Table S42: LIBS elemental analyses of "white" particles (15 scans); Table S43: LIBS elemental analyses of PA6 reference (15 scans); Table S44: LIBS elemental analyses of mussel-shell reference (15 scans); Table S45: TGA raw data of U70/30 filament after immersion (n = 5); Table S46: TGA raw data of U70/30 test specimen after immersion (n = 5); Table S47: TGA raw data of U80/20 filament after immersion (n = 5); Table S48: TGA raw data of U80/20 test specimen after immersion (n = 5); Table S49: TGA raw data of U90/10 filament after immersion (n = 5); Table S50: TGA raw data of U90/10 test specimen after immersion (n = 5); Table S51: Mixing ratios of all formulations before and after immersion (filaments and test specimens, n = 5); Table S52: ANOVA: immersion test—mixing ratio of filaments; Table S53: Levene's test: immersion test—mixing ratio of filaments; Table S54: Tukey's HSD: immersion test—mixing ratio of filaments; Table S55: ANOVA: immersion test—mixing ratio of test specimens; Table S56: Levene's test: immersion test—mixing ratio of test specimens; Table S57: Tukey's HSD: immersion test—mixing ratio of test specimens.

Author Contributions: Conceptualization, J.T., T.P. and M.E.; methodology, J.T.; software, J.T.; validation, J.T., T.P. and M.E.; formal analysis, J.T.; investigation, J.T.; resources, J.T.; data curation, J.T.; writing—original draft preparation, J.T.; writing—review and editing, T.P. and M.J.; visualization, J.T.; supervision, T.P.; project administration, M.E.; funding acquisition, T.P. All authors have read and agreed to the published version of the manuscript.

Funding: This research was conducted within the project "Prevention, reduction and recycling of fishnets polluting Vietnamese coastal waters (REVFIN)", funded by the Federal Ministry for the Environment, Nature Conservation, Nuclear Safety and Consumer Protection (BMUV Funding No. 67MM0007) on the basis of a resolution of the German Bundestag.

Institutional Review Board Statement: Not applicable. This study did not involve humans or animals.

Data Availability Statement: The data presented in this study are available on request.

Acknowledgments: During the preparation of this manuscript, the authors used OpenAI GPT-6 for the refinement of English, manuscript structuring, and scientific language correction. The authors have reviewed and edited the output and take full responsibility for the content of this publication.

Conflicts of Interest: The authors declare no conflicts of interest.

Abbreviations

The following abbreviations are used in this manuscript:

AM	Additive Manufacturing
ANOVA	Analysis of Variance
ASTM	American Society for Testing and Materials
$CaCO_3$	Calcium Carbonate
DIN	Deutsches Institut für Normung (German Institute for Standardization)
DSC	Differential Scanning Calorimetry
FDM	Fused Deposition Modeling
HSD	Honestly Significant Difference
ISO	International Organization for Standardization
LIBS	Laser-Induced Breakdown Spectroscopy
PA6	Polyamide 6
SD	Standard deviation
SSbD	Safe and sustainable by Design
SEM	Scanning Electron Microscopy
TGA	Thermogravimetric analysis
µCT	Micro-Computed Tomography

References

1. van den Brink, A.; Fomsgaard, C.; Nedelec, M.; Hussenot, M.; Kamermans, P. *OYSTERECOVER: Testing the Efficiency of Different Spat Collectors*; C216/13; IMARES: Brussels, Belgium, 2013.
2. Buitrago, E.; Alvarado, D. A highly efficient oyster spat collector made with recycled materials. *Aquac. Eng.* **2005**, *33*, 63–72. [CrossRef]
3. Hingant, M.; Mallarino, S.; Conforto, E.; Dubillot, E.; Barbier, P.; Bringer, A.; Thomas, H. Artificial weathering of plastics used in oyster farming. *Sci. Total Environ.* **2023**, *868*, 161638. [CrossRef] [PubMed]
4. Azarian, H.; Sutapun, W. Biogenic calcium carbonate derived from waste shells for advanced material applications: A review. *Front. Mater.* **2022**, *9*, 1024977. [CrossRef]
5. Benaichouba, Z.; Bachir Bouiadjra, B.A.; Mokhtar Bouziane, M.; Khaldi, M.; Singh, M.K.; Palaniappan, S.K. Upcycling Oyster Shell Waste into Sustainable Polypropylene Biocomposites: Synthesis and Characterization. *J. Compos. Sci.* **2025**, *9*, 674. [CrossRef]
6. Owuamanam, S.; Cree, D. Progress of Bio-Calcium Carbonate Waste Eggshell and Seashell Fillers in Polymer Composites: A Review. *J. Compos. Sci.* **2020**, *4*, 70. [CrossRef]
7. Bouiadjra, B.A.; Albedah, A.; Mohammed, S.; Abdo, H.; Alothman, O.; Bouziane, M.M. Thermal stability and mechanical characterization of oyster shell reinforced recycled polypropylene biocomposite. *J. Reinf. Plast. Compos.* **2024**, *44*, 2969–2980. [CrossRef]
8. Shah, A.u.R.; Prabhakar, M.N.; Wang, H.; Song, J.-I. The influence of particle size and surface treatment of filler on the properties of oyster shell powder filled polypropylene composites. *Polym. Compos.* **2018**, *39*, 2420–2430. [CrossRef]
9. Qu, C.-L.; Lin, S.-M.; Potiyaraj, P.; Meng, L.; Wu, C.-S.; Yuan, L.; Luo, X.; Ge, F.-F.; Tsou, C.-H. Polymer Packaging through the Blending of Biowaste Oyster Shell and Low-Density Polyethylene: A Sustainable Approach for Enhanced Food Preservation. *Polymers* **2023**, *15*, 3977. [CrossRef] [PubMed]
10. Theobald, B.; Risani, R.; Donaldson, L.; Bridson, J.H.; Kingsbury, J.M.; Pantos, O.; Weaver, L.; Lear, G.; Pochon, X.; Zaiko, A.; et al. An investigation into the stability and degradation of plastics in aquatic environments using a large-scale field-deployment study. *Sci. Total Environ.* **2024**, *917*, 170301. [CrossRef] [PubMed]
11. Costa, M.V.A.; Magrinho, J.P.G.; Caseiro, J.F.M.; Pires, A.L.L.; Fidelis, N.; Silva, M.B. Analysis of the Feasibility of Producing Injection Moulded Components from Mechanically Recycled Fishing Nets. *Key Eng. Mater.* **2023**, *957*, 71–79. [CrossRef]

12. Kohutiar, M.; Kakošová, L.; Krbaťa, M.; Janík, R.; Fekiač, J.; Breznicka, A.; Eckert, M.; Mikuš, P.; Timárová, Ľ. Comprehensive Review: Technological Approaches, Properties, and Applications of Pure and Reinforced Polyamide 6 (PA6) and Polyamide 12 (PA12) Composite Materials. *Polymers* **2025**, *17*, 442. [CrossRef] [PubMed]
13. Lu, J.; Cong, X.; Li, Y.; Hao, Y.; Wang, C. Scalable recycling of oyster shells into high purity calcite powders by the mechanochemical and hydrothermal treatments. *J. Clean. Prod.* **2018**, *172*, 1978–1985. [CrossRef]
14. Nwanonenyi, S.; Obidiegwu, M.; Onuchukwu, T.S.; Egbuna, I.C. Studies on the Properties of Linear Low Density Polyethylene Filled Oyster Shell Powder. *Int. J. Eng. Sci. IJES* **2013**, *2*, 42–48.
15. Harikumar, A.A.; Heitzmann, M.; Basnayake, A.; Khakbaz, H.; Martin, D. Tribological Performance of Nylon-6/Oyster Shell Composites. In Proceedings of the ASME 2023 42nd International Conference on Ocean, Offshore and Arctic Engineering, Melbourne, Australia, 11–16 June 2023. [CrossRef]
16. Sharvesh, R.; Babu, M.; Soundararajan, R. Appraisal of Mechanical and Tribological Behaviour of Polyamide 6 with Carbon Fibre-Filled Composites Fabricated Through Fused Deposition Modelling. *J. Inst. Eng. India Ser. D.* **2025**, *106*, 1483–1492. [CrossRef]
17. Romario, Y.S.; Octavia, T.; Hananto, T.; Xaverius, F. Sustainable Composite Fabrication Using Waste Oyster Shells Through Additive Manufacturing Technology. *J. Chin. Soc. Mech. Eng.* **2024**, *045*, 501–507.
18. Reins, L.; Wijns, J. The "Safe and Sustainable by Design" Concept—A Regulatory Approach for a More Sustainable Circular Economy in the European Union? *Eur. J. Risk Regul.* **2025**, *16*, 96–113. [CrossRef]
19. Caldeira, C.; Garmendia, A.I.; Tosches, D.; Mancini, L.; Abbate, E.; Farcal, R.; Lipsa, D.; Rasmussen, K.; Rauscher, H.; Riego, S.J.; et al. *Safe and Sustainable by Design Chemicals and Materials—Application of the SSbD Framework to Case Studies*; JRC Technical Report; Publications Office of the European Union: Luxembourg, 2023. [CrossRef]
20. Apel, C.; Kümmerer, K.; Sudheshwar, A.; Nowack, B.; Som, C.; Colin, C.; Walter, L.; Breukelaar, J.; Meeus, M.; Ildefonso, B.; et al. Safe-and-sustainable-by-design: State of the art approaches and lessons learned from value chain perspectives. *Curr. Opin. Green. Sustain. Chem.* **2024**, *45*, 100876. [CrossRef]
21. Transforming Our World: The 2030 Agenda for Sustainable Development|Department of Economic and Social Affairs. n.d. Available online: https://sdgs.un.org/2030agenda (accessed on 12 June 2026).
22. Moneke, M. *Kunststoffwerkstoffe: Fachbuch für Lehre und Praxis*; Hanser: München, German, 2022.
23. Ehrenstein, G.W.; Pongratz, S. *Beständigkeit von Kunststoffen*; Hanser Verlag: München, German, 2007. [CrossRef]
24. Coote, G.E.; Trompetter, W.J. Proton microprobe studies of fluorine distributions in mollusc shells. *Nucl. Instrum. Methods Phys. Res. Sect. B Beam Interact. Mater. At.* **1995**, *104*, 333–338. [CrossRef]
25. Baur, E.; Drummer, D.; Osswald, T.A.; Rudolph, N. *Saechtling Kunststoff-Handbuch*, 32nd ed.; Carl Hanser Verlag GmbH & Co. KG: München, German, 2022. [CrossRef]
26. Kantaros, A.; Soulis, E.; Petrescu, F.; Ganetsos, T. Advanced Composite Materials Utilized in FDM/FFF 3D Printing Manufacturing Processes: The Case of Filled Filaments. *Materials* **2023**, *16*, 6210. [CrossRef] [PubMed]
27. Ehrenstein, G.W. *Polymer-Werkstoffe: Struktur—Eigenschaften—Anwendung. 3. Auflage*; Hanser: München, German, 2011. [CrossRef]
28. Renganathan, S.; DS. Effect of fill pattern and printing speed on friction characteristics of FDM printed polylactic acid polymer. *Adv. Mater. Process Technol.* **2022**, *8*, 1583–1592. [CrossRef]

Disclaimer/Publisher's Note: The statements, opinions and data contained in all publications are solely those of the individual author(s) and contributor(s) and not of MDPI and/or the editor(s). MDPI and/or the editor(s) disclaim responsibility for any injury to people or property resulting from any ideas, methods, instructions or products referred to in the content.